MIS 5e relative sea-level changes in the Mediterranean Sea

Contribution of isostatic disequilibrium

Stocchi, Paolo; Vacchi, Matteo; Lorscheid, Thomas; de Boer, Bas; Simms, Alexander R.; van de Wal, Roderik S W; Vermeersen, Bert L.A.; Pappalardo, Marta; Rovere, Alessio

DOI
10.1016/j.quascirev.2018.01.004

Publication date
2018

Document Version
Accepted author manuscript

Published in
Quaternary Science Reviews

Citation (APA)
Stocchi, P., Vacchi, M., Lorscheid, T., de Boer, B., Simms, A. R., van de Wal, R. S. W., Vermeersen, B. L. A., Pappalardo, M., & Rovere, A. (2018). MIS 5e relative sea-level changes in the Mediterranean Sea: Contribution of isostatic disequilibrium. *Quaternary Science Reviews*, *185*, 122-134. https://doi.org/10.1016/j.quascirev.2018.01.004

MIS 5e relative sea-level changes in the Mediterranean Sea: contribution of isostatic disequilibrium

Paolo Stocchi[1,*], Matteo Vacchi[2,3], Thomas Lorscheid[4,5], Bas de Boer[6], Alexander R. Simms[7], Roderik van de Wal[6], Bert L.A. Vermeersen[8,9], Marta Pappalardo[10], Alessio Rovere[4,5]

[1]NIOZ - Royal Netherlands Institute for Sea Research, Coastal Systems (TX), and Utrecht University, P.O. Box 59, 1790 AB, Den Burg, Texel, The Netherlands

[2]Université P. Valéry Montpellier 3, CNRS ASM, UMR 5140, 34970 Montpellier, France

[3]Geography, College of Life and Environmental Sciences, University of Exeter, Exeter EX44RJ, UK.

[4]MARUM - Center for Marine Environmental Sciences, University of Bremen, Leobener Straße 8, 28359, Bremen, Germany

[5]ZMT - Leibniz Centre for Tropical Marine Research, Fahrenheitstraße 6, 28359 Bremen, Germany

[6]IMAU – Institute for Marine and Atmospheric research Utrecht, Utrecht University, Utrecht, The Netherlands

[7]University of California Santa Barbara, Santa Barbara (CA), USA

[8]NIOZ - Royal Netherlands Institute for Sea Research, Estuarine and Deltaic Systems (YK), and Utrecht University, Korringaweg 7, 4401 NT, Yerseke, The Netherlands

[9]TU Delft, Faculty of Aerospace Engineering, Delft, The Netherlands

[10]Università di Pisa, Dipartimento di Scienze della Terra, Pisa, Italy

[*]Corresponding author

Abstract

Sea-level indicators dated to the Last Interglacial, or Marine Isotope Stage (MIS) 5e, have a twofold value. First, they can be used to constrain the melting of Greenland and Antarctic Ice Sheets in response to global warming scenarios. Second, they can be used to calculate the vertical crustal rates at active margins. For both applications, the contribution of glacio- and hydro-isostatic adjustment (GIA) to vertical displacement of sea-level indicators must be calculated. In this paper, we re-assess MIS 5e sea-level indicators at 11 Mediterranean sites that have been generally considered tectonically stable or affected by mild tectonics. These are found within a range of elevations of 2-10 m above modern mean sea level. Four sites are characterized by two separate sea-level stands, which suggest a two-step sea-level highstand during MIS 5e. Comparing field data with numerical modeling we show that (i) GIA is an important contributor to the spatial and temporal variability of the sea-level highstand during MIS 5e, (ii) the isostatic imbalance from the melting of the MIS 6 ice sheet can produce a >2.0 m sea-level highstand, and (iii) a two-step melting phase for the Greenland and Antarctic Ice Sheets reduces the differences between observations and predictions. Our results show that assumptions of tectonic stability on the basis of the MIS 5e records carry intrinsically large uncertainties, stemming either from uncertainties in field data and GIA models. The latter are propagated to either Holocene or Pleistocene sea-level reconstructions if tectonic rates are considered linear through time.

Keywords: Pleistocene; Sea Level changes; Europe; Geomorphology, coastal

1. Introduction

Sea-level changes are primarily a reflection of water mass transfer between continents, where water is stored as ice during cold periods, and oceans, where meltwater is introduced during warmer periods. This process is known as glacial eustasy (Suess, 1906) and occurs in response to changes in atmosphere and ocean temperatures related to variations in atmospheric CO_2 concentrations and Milankovitch-driven insolation (Stocker et al., 2013). A fundamental aspect for the study of past climate change over glacial-interglacial time scales is the collection, analysis and interpretation of

Relative Sea Level (RSL) indicators, that are fossil landforms, deposits or biological assemblages with a known relationship with a paleo sea level (Hibbert et al., 2016; Rovere et al., 2016a). Once vertical movements associated with Glacial Isostatic Adjustment (GIA) (Lambeck and Purcell, 2005), tectonics (Simms et al., 2016) or other post-depositional processes (Rovere et al., 2016b) are taken into account, paleo RSL indicators can be used to constrain ice-mass variations in response to changes in atmospheric and ocean temperatures during past interglacials (Dutton et al., 2015). In turn, estimates of paleo global mean sea level can be used to constrain processes regulating ice melting in paleo ice-sheet models, which eventually may be used to gauge the sensitivity of present-day polar ice sheets to future scenarios of global warming (e.g. DeConto and Pollard, 2016).

The most studied past interglacial is the Marine Isotopic Stage 5e (MIS 5e, 117-127 ka), which is the last period of the Earth's history when climate was warmer than today. Generally, MIS 5e sea-level studies are oriented towards two main goals. The first is to understand how to account for processes causing departures from eustasy (e.g., GIA, tectonics) in order to produce reliable estimates of past global mean sea levels. The second consists on the calculation of tectonic movements starting from the elevation of RSL indicators and assumptions on eustatic sea-level changes. This aspect is particularly relevant for the understanding of the long-term vertical movement of coastal areas, which is in turn important for the planning of coastal infrastructures in active geodynamic settings and need to be accounted for to correct future climate-related rates of RSL change (Antonioli et al., 2017).

Despite the common consideration in isolation, the two aims outlined above are mutually dependent and they are both tied to GIA predictions. In fact, to achieve the second goal, one must calculate the climate-related and GIA-modulated RSL elevations, which are the result of the first goal. The latter, however, stems from *a priori* information on long-term tectonic motions, which is the result of this second goal. Studies on MIS 5e RSL change in the Mediterranean Sea have often either adopted standard ESL values to calculate vertical tectonic rates at active sites or neglected the GIA overprint in the calculation of the ESL signal (Ferranti et al., 2006).

In this paper we focus on MIS 5e sea-level variations in the Mediterranean Sea. We investigate the GIA contributions to the spatiotemporal variability of RSL change during MIS 5e within the basin

using GIA numerical simulations that incorporate the solid Earth and gravitational response to three glacial-interglacial cycles prior to MIS 5e and that evolve towards present. We also evaluate the GIA-modulated contribution of four scenarios for GrIS and AIS melting during MIS 5e. We compare our RSL predictions to observations from 11 sites that have been previously hypothesized as tectonically stable based on the low elevation of the MIS 5e shoreline.

We use field data and numerical GIA predictions at these sites to address the following questions:

1. How much of the observed MIS 5e RSL variability in the Mediterranean can be explained by GIA?
2. How significant are the uncertainties in GIA, as well as GrIS and AIS melting scenarios when using MIS 5e shorelines to calculate tectonic vertical motions?

2.Materials and methods

2.1 Paleo Relative Sea-level indicators

The Mediterranean Sea has been a central focus for studies on sea level changes for over two centuries (Benjamin et al., 2017). The basin is characterized by different tectonic regimes (Figure 1, see Supplementary Text for a brief outline) and its relatively low tidal amplitudes and low wave energy helped to preserve RSL indicators almost ubiquitously (see Figure 1 in Ferranti et al., 2006 for an overview and detailed reports in Anzidei et al., 2014; Ferranti et al., 2006; Galili et al., 2007; Mauz et al., 2012; Pedoja et al., 2014).

In the absence of MIS 5e reefs (Dutton and Lambeck, 2012; Hibbert et al., 2016), the main Mediterranean Pleistocene RSL indicators can be divided into three main categories: i) Depositional, consisting mostly of cemented beach or shallow marine deposits (Figure 2a-c,e,f). ii) Biological, consisting of fossil remains of benthic organisms living attached to hard substrates (Rovere et al., 2015) or traces of bioeroding organisms (e.g. *L. lithophaga* boreholes, Figure 2d). iii) Geomorphological: all landforms formed by the action of the sea over time. Typical geomorphological MIS 5e markers include fossil shore platforms or tidal notches (Figure 2d, f, Antonioli et al., 2015). Often, dating of Mediterranean MIS 5e RSL indicators is challenging because the preservation of *in situ* corals for U-series measurements is rare.

113 To calculate the paleo RSL from the measured elevation of a RSL indicator, it is essential to
114 decouple the actual measured elevation of the indicator and the interpretation of the paleo sea level
115 that it represents (Düsterhus et al., 2016). This is done by subdividing the measured elevation,
116 which should be done at the highest possible accuracy and should always be referenced to a tidal
117 datum, and the indicative meaning of the RSL indicator (Shennan, 1982,1989; Hijma et al., 2015;
118 Shennan et al., 2014; Shennan and Horton, 2002; Van de Plassche, 1986). The indicative meaning
119 is composed of the indicative range (IR, the range over which an indicator forms, e.g. from the
120 uppermost tide to the mean lowest tide) and the reference water level (RWL, the midpoint of the
121 indicative range) (see Vacchi et al., 2016 for examples on Holocene Mediterranean RSL indicators).
122 In this study, we assess the elevation and indicative meaning of MIS 5e RSL indicators from 11
123 sites among the most representative for the Mediterranean (Figure 1). To calculate paleo RSL from
124 the elevation of RSL indicators we followed the approach and formulas suggested by Rovere et al.,
125 2016a. Figure 2 shows geological sketches (a-f) and pictures of sites 5,6 and 11 (f,d,b,
126 respectively). In the Supplementary Materials, we present a spreadsheet with details on how the
127 indicative meaning has been calculated at each site and a text file including an example of paleo
128 RSL calculation for Cala Mosca (site 8, Figure 2c). At sites 3 and 6 the elevation was re-measured
129 with high-accuracy differential GPS (Trimble ProXRT receiver and Trimble Tornado antenna
130 receiving OmniSTAR HP+G2 real-time corrections) and referred to mean sea level using local tidal
131 datums. For the remaining sites, the elevation of the RSL indicators and its accuracy were extracted
132 from published data.
133
134 *2.2 Glacial- and hydro-isostatic adjustment (GIA)*
135 The GIA process is formally described by the linear and integral Sea Level Equation (SLE; Farrell
136 and Clark, 1976). Solving the SLE for a prescribed ice-sheet model and solid Earth rheological
137 model yields the gravitationally self-consistent RSL changes on a global scale and as a function of
138 time. We solve the SLE by means of the SELEN program (Spada and Stocchi, 2007), which uses
139 the pseudo-spectral method (Mitrovica and Peltier, 1991) and includes solid the Earth rotation, the
140 shift of the center of mass of the Earth as well as the migration of coastlines (time-dependent ocean

function). We employ a spherically symmetric, radially stratified, deformable but non-compressible, self-gravitating and rotating solid Earth model. The physical and rheological parameters depend on the radius only, which implies that the rheological model is 1D. We assume a purely elastic lithosphere (outer shell) and keep its thickness fixed to 100 km. The mantle is discretized in three layers, which are characterized by a linear Maxwell viscoelastic rheology, and are called, from top to bottom, Upper Mantle (UM), Transition Zone (TZ) and Lower Mantle (LM). We compare the performance of three different mantle viscosity profiles (MVP) that are characterized by an increase of viscosity gradient from top to bottom (see Table 1 for details)

2.2.1 MIS 5e glacioeustatic scenarios

We make use of the existing global ice-sheet model that was generated by De Boer et al. (2014) by using ANICE-SELEN coupled ice-sheet -- sea-level model. The model describes ice-sheets thickness variation for the last 410 ka and consists of a system of four 3-D regional ice-sheet-shelf models (Eurasia, North America, Greenland and Antarctica) that simulate ice flow with a combination of shallow ice and shelf approximations (de Boer et al., 2014). The topography variations that accompany ANICE-SELEN simulations account for the GIA-induced RSL changes that follow from the solution of the SLE (Spada and Stocchi, 2007). In the ANICE-SELEN model, the four regional ice-sheet models and the induced RSL changes, which in turn drive the topographic variations, are run simultaneously and coupled at every time-step. Hence, the four regional ice-sheet models fully and dynamically incorporate all the GIA feedbacks described by the SLE.

We follow the original ice-sheet chronology starting from 410 ka through the MIS 6 glacial maximum and match the end of MIS 6 Eurasia and North America ice sheets's deglaciation at 127 ka. By the same time, the thickness of Greenland and Antarctic Ice Sheets (GrIS and AIS, respectively) are scaled to reach the present-day volume, which implies a eustatic sea level of 0.0 m above present-day sea level. We keep the GrIS and AIS thicknesses constant between 127 and 116 ka. After 126 ka, the four ice sheets follow the original simulation presented in De Boer et al. (2014) and undergo the fourth (and last) glacial-interglacial cycle. We call this model "background

model" and the associated GIA response between 127 and 116 ka "background GIA", implying that it accounts for the GIA contribution of the three glacial-interglacial cycles previous to MIS 5e interglacial.

Subsequently, the melting of the GrIS and AIS between 127 and 116 ka is over-imposed to the background model according to the following four scenarios (see Figure 3):

- *Scenario 1.* This scenario reflects the traditional view of MIS 5e sea-level history, with the melting of both GrIS (2.0m) and AIS (5.0m) occurring early in the interglacial, and not changing until insolation in both hemispheres decreases and glacial conditions start to resettle (see Figure 3).
- *Scenario 2.* This scenario includes a two-step highstand. However, the GrIS contributes 2.0 m of ESL equivalent between 127 and 116 ka while the AIS contributes 5.0m only after 120 ka (Figure 3).
- *Scenario 3.* The GrIS and AIS release, respectively, 2.5 and 1.0 m ESL at 127 ka. GrIS remains stable until 116 ka, while AIS releases 4.5 m ESL after 120 ka (Figure 3). The two-step retreat of GrIS and AIS, therefore, results in a maximum eustatic peak of 8.0 m between 119 and 117 ka. Scenarios 2 and 3 are in line with the timing and magnitudes proposed by O'Leary et al. (2013).
- *Scenario 4.* This scenario is chronologically opposite to the scenario and at odds with O'Leary et al. (2013). The GrIS and AIS melt to their maximum extent early in the interglacial, and ice formation is forced in Antarctica towards the end of MIS 5e (Figure 3).

2.2.2 Numerical predictions

We compute, evaluate and discuss *(i)* maximum RSL elevations along a transect that connects the 11 sites of Figure 1, *(ii)* RSL curves at each site, RSL changes across the whole Mediterranean Sea (maps), *(iii)* differences between observed and predicted RSL elevations

3. Results

3.1 RSL data

197 The difference between the measured elevation of the RSL indicators and the actual paleo sea level
198 can be significant once the indicative meaning is properly accounted for (Figure 2g, see
199 Supplementary Materials for details on the calculation of the indicative meaning at each site and the
200 Supplementary Text for a working example). The set of 11 revised RSL sites from supposedly
201 stable areas in the Mediterranean shows a MIS 5e RSL highstand in the range of 2-10 m above
202 present-day sea level (Figure 2g). Two distinct elevations of the MIS 5e sea level are locally
203 recorded at Mallorca, Tyrrhenian Sea, Sardinia and Tunisia (Figure 2g, sites no.3,5,8 and 9).
204
205 *3.2 Background GIA in the Mediterranean*
206 The background GIA contributes to a generalized RSL highstand during MIS 5e that is
207 characterized by a significant spatial variability (Figure 4). According to MVP1 (red curve in
208 Figure 4), a maximum RSL elevation of ~2.0 m is predicted at site no. 1 (Al Hoceima, Morocco),
209 while for the other sites the predictions fall within a range of 0.5 and 1.25 m above present-day sea
210 level. The larger gradient between UM and LM viscosity, which characterizes MVP2, yields higher
211 high-stands in the central Mediterranean sites, while the RSL elevation at site no.1 reduces to ~1.3
212 m (green curve in Figure 4). A further increase in the viscosity gradient UM and LM, as described
213 by MVP3, exacerbates this pattern and results in a higher RSL elevation in the central
214 Mediterranean, while a reduction occurs at sites no.1 and no.11 (blue curve in Figure 4). The
215 absolute maximum high-stand (> 2.0 m) is predicted at sites no.7 and 8 (Sardinia, Italy) for MVP3
216 (Figure 4). This value is comparable to the glacioeustatic contribution of the GrIS as proposed so
217 far.
218 The predicted maximum RSL highstands of Figure 4 occur at different times as a function of the
219 geographic location (see Figure 5 a-c). At site no. 1 (Al Hoceima, Morocco; solid red curve in
220 Figure 5a), MVP1 results in a RSL rise ~2.0 m above present-day sea level between 125 and 126
221 ka. This is followed by a RSL drop that reaches present-day sea level at 116 ka. According to
222 MVP1 and moving eastwards along the transect (i.e. towards the center of the basin), the predicted
223 RSL curves are characterized by lower high-stands that occur later in time. At site no. 4 (Bergeggi,
224 Italy; dotted red curve in Figure 5a) the predicted RSL exceeds present-day sea level after 125 ka.

225 i.e. 2.0 ka later than at site no. 1, while the maximum elevation occurs 3.0 ka later. At site no. 5
226 (Cala Mosca, Sardinia, Figure 5a) the predicted maximum RSL elevation occurs by 116 ka.
227 Results for MVP2 show a reduction of the maximum RSL elevation at western and eastern sites and
228 steeper RSL curves (i.e. higher RSL rates; Figure 5b). According to MVP3, the maximum elevation
229 is attained at site 8 (Cala Mosca, Sardinia) at 116 ka (dashed curve in Figure 5c), while site no.1
230 experiences a high-stand peak that is half the MVP1 prediction and that occurs 6-7 ka later (solid
231 curve in Figure 5c).
232
233 To investigate the role of the water-loading term and its interaction with the solid Earth we perform
234 the same simulations of Figures 4 and 5 but neglecting the ice-loading contribution for the whole
235 background model (Background GIA – Ocean loading, see Figure 6a). Therefore, when ice sheets
236 grow (or shrink), water is taken from (or placed to) the oceans without being compensated by ice
237 loads on the continents. The predicted maximum RSL elevations are largely different from the
238 standard background GIA solutions (Figure 6a). The spatial variability of the RSL change is
239 significantly reduced. The sites located in the center of the basin (no.3, and no.5-8) together with
240 the three sites along North Africa (no.9-11) experience a maximum RSL rise that is close to the
241 eustatic value (i.e. 0.0 m above present-day sea level). A maximum RSL elevation of ~0.5 m is
242 predicted at sites no.7 and 8 (Sardinia) for MVP1 (red dots in Figure 6). The maximum elevation
243 decreases with the increasing viscosity gradient between UM and LM in MVP2 and MVP3. This
244 trend is generally opposite to the standard background GIA, where the maximum RSL elevation is
245 calculated for MVP3 (see Figure 4). The maximum RSL elevations are predicted, with decreasing
246 height, at sites no.1, 2 and 4. Also here, as well as at sites no.7 and 8, the viscosity profile has an
247 opposite effect with respect to the standard background GIA solutions of Figure 4. Similarly to the
248 latter, the maximum RSL elevations occur at different times according to the geographical location
249 (solid curves in Figure 6c-h). At sites no.1 and 4 (Figure 6c and d, respectively), the maximum
250 highstand occurs at 127 ka. which corresponds to the end of MIS 6 ice-sheets deglaciation. For all
251 the three mantle viscosity profiles, the highstands are followed by a RSL drop that closely resemble
252 the standard background GIA prediction for MVP1 at site no.1 (see Figure 5a). Conversely, an

almost monotonous RSL rise characterizes the predictions at the central sites no.6 and 8 between 127 and 116 ka (Figure 6e, f). Lower positive RSL rates are predicted at sites no.10 and 11 (Figure 6g, h), where the curves are very close to eustatic.

Neglecting the ice-loading term of the Eurasian aggregate only results in an upward shift of 0.5-1.0 m of the maximum predicted RSL at sites no. 3 and no. 5-11 (Background GIA – Partial ocean loading, see Figure 6b) and with respect to the background GIA – Ocean loading (Figure 6a). At sites no. 1,2 and 3, instead, the maximum elevations are 0.5-1.0 m lower than the background GIA – Ocean loading . The effect of the mantle viscosity profile is in line with the standard background GIA (Figure 4, 5). In fact, the RSL highstand increases in the center of the Mediterranean basin (sites no.3, 7 and 9) when moving from MVP1 to MVP3. The opposite occurs at sites no.1, 2 and 4. The predicted RSL curves at sites no. 1 and 4 are characterized by a lower early highstand peak at 127 ka and by a longer duration of the RSL drop phase (dashed curves in Figure 6c,d). At sites no. 6 and 8 (Figure 6e, f), the ice-loading term results in ~1.0 m highstand between 121 and 116 ka. Similarly to sites no.1 and 4, an early peaked highstand is obtained at sites no. 10 and 11 (Figure 6g, h).

3.3 Scenarios 1-4

Our results account for the background GIA as well as for the GIA that accompanies and follows AIS and GrIS melting during MIS 5e, according to scenarios 1-4 (Figure 3a-d). Figure 7a shows the predicted RSL (with respect to present-day) at 122 ka according to scenario 1 and MVP1. A RSL elevation that is ~0.5-1.0 m higher than eustatic (7.0 m) is already attained by 122 ka along most of the northern coastlines (Figure 7a) and in southern Spain (site no. 2) and Morocco (site no. 1). At sites no. 3, 7 and 8 a maximum value of ~6.0 m is predicted. Therefore, a maximum difference of ~1.5 m is predicted between the coastal areas and the center of the Mediterranean basin, where the background GIA results in a delay in the appearance of the highstand.

Predictions for MVP2 (Figure 7b) and MVP3 (Figure 7c) reveal the role of mantle viscosity profile and, in particular, of the viscosity contrast between UM and LM. According to MVP2, values equal

281 to or 0.5 m higher than the eustatic remain in southeastern Spain and Morocco. At sites no. 3-8 a
282 maximum value of 5-6 m is predicted. Therefore a maximum ~2.5 m difference exists between the
283 center of the Mediterranean basin and the southeastern coasts. This trend increases when moving to
284 MVP3, which in fact results in a further delay of the MIS 5e highstand (Figure 7c).
285
286 The predicted RSL curves for scenario 1 and MVP2 show that, by 122 ka (Figure 8), the RSL is
287 dropping at site no. 1, while at sites no. 4, 5, 7 and 8, it is still rising towards the maximum
288 elevation, which then occurs by 116 ka. The predicted RSL trend at site no.1 and between 122 and
289 116 ka is at odds with the predictions at site no.7. Opposite RSL trends are also predicted at
290 different sites for scenarios 2 and 3 (Figure 8, black and pink curves). This holds in particular
291 between 119 and 117 ka, i.e. after meltwater is released from the AIS (see Figure 3b,c). Both
292 scenarios 3 and 4 result in a maximum highstand peak of 8 m, which occurs between 119 and 117
293 ka according to scenario 3 and between 127 and 120 ka according to scenario 4.
294 Our results show that, when scenario 3 is combined with MVP2, the maximum eustatic peak is
295 reached and even surpassed by 119 ka at sites 4, 5, 7 and 10. Instead, the role of background GIA
296 inhibits the appearance of the maximum peak when scenario 4 is considered. This stems from the
297 delayed subsidence of the sea bottom in response to the melting of MIS 6 ice-sheets.
298
299 To quantify the differences between predictions and observations we make a heuristic use of the
300 chi-square merit function:

301 $$\chi^2 = \frac{1}{N} \sum_{i=1}^{N} \frac{\left(S_i^o - S_i^p\right)^2}{\left(\sigma_i^o\right)^2} \qquad \text{Eq. (1)}$$

302 where N is the number of observations, S_i^o is the paleo RSL elevation obtained from field data and
303 considerations on the indicative meaning as described in this paper, σ_i^o is the standard deviation of
304 the observation and S_i^p is the predicted maximum sea level. We first assume that the sea-level
305 observations at the 11 sites considered in this study represent the maximum elevations attained by
306 the sea level during MIS 5e. At the four sites that record two different sea-level stands (Figure 2),

307 we neglect the lower stand and consider the higher elevation only. We predict the highest elevation
308 reached by sea level during MIS 5e according to scenarios 1-4 and MVP 1-3 at each site and then
309 compute the χ^2 (see Eq. 1). Scenario 3 stands out clearly as the worst solution for each of the three
310 mantle viscosity profiles (see Figure 9a). The relatively large misfit mostly stems from the
311 difference between predicted and observed low sea level at site no. 11 (Israel). The latter suggests
312 that each observation does not necessarily correspond to the local maximum highstand attained
313 during MIS 5e. However, the lack of reliable dating techniques prevents a more detailed
314 comparison between data and predictions.
315 Secondly, we assume that the observed RSL indicators that are below +5.0 m represent a lower
316 highstand, while those above +5.0 m indicate a higher sea-level stand (which might be the
317 maximum MIS 5e local highstand). To locate the events in time we assume that the lower
318 highstands (<= 5.0 m) occurred before120 ka, while the higher occurred after 120 ka. Accordingly,
319 at sites where one sea level only is observed, we assume that it represents either the lower or the
320 higher highstand. At sites where two different sea levels are observed, these record two consecutive
321 highstands. To compare predictions with the observations, we calculate the maximum peaks before
322 and after 120 ka and compare them, respectively, to the lower and higher observed elevations. For
323 Scenario 4 (see Figure 3) we invert the chronological order of the peaks. The comparison between
324 data and predictions (Figure 9b) reveals that scenario 1 is now the least appropriate, being not able
325 to satisfactorily fit a two-step signal. Scenario 3 and 4 are equivalent.
326
327 *3.4 Tectonic stability from MIS 5e RSL histories*
328 The previous sections show that field data, glacioeustatic scenarios and GIA calculations bring
329 large uncertainties in the reconstruction of MIS 5e sea-level history. These uncertainties must be
330 reflected in tectonic estimates from MIS 5e sea-level observations. In this paragraph we use the
331 field data, GIA and glacioeustatic scenarios (and their uncertainties) described above to answer the
332 question: how significant are field-related, GIA and eustatic sea-level uncertainties when attempting
333 to use MIS 5e shorelines to calculate tectonic vertical deformations?

To answer this question, we use the following equation to calculate uplift/subsidence rates from MIS 5e sea-level histories:

$$PDr = \left[\frac{S_T^o - S_T^p}{T}\right] \qquad \text{Eq. (2)}$$

Where PDr is the post-depositional rate of uplift (positive) or subsidence (negative), S_T^o is the observed paleo RSL (see also Eq. 1), S_T^p is the predicted sea level that stems from Scenarios 1-4 (see Figure 8) and T is time. At each site, we reiterate 1000 solutions of Eq.2 for each time step (each 100 years between 116 and 126 ka, n=11) and for each GIA model and eustatic scenario (n=12), randomly sampling a Gaussian distribution where μ is the paleo RSL at each site and δ is the associated paleo RSL uncertainty to represent S_T^o. We calculate 132,000 possible *PDr* rates, that we plot using simple histograms (blue histograms in Figure 10). We compare this solution with a simpler solution of Eq.2 where, instead of accounting for GIA, we set S_T^p equal to 6 meters, a value often considered as representative of MIS 5e ESL (gray histograms in Figure 10). Although it is possible to affirm that all the 11 sites are characterized by mild rates of tectonic motions, the uncertainties surrounding such assumptions are relevant when GIA and different ESL scenarios are considered (Figure 10).

4. Discussion

Our numerical simulations show that the Earth is not in isostatic equilibrium during the MIS 5e. The GIA processes that accompany and follow the melting of GrIS and AIS during the MIS 5e (scenarios 1-4) add up to the background GIA to increase the regional RSL variability. Each location, within the Mediterranean Sea and during MIS 5e, is characterized by a local RSL curve that can be significantly different from the eustatic.

The GIA-induced spatial variability of the RSL change is small if compared to the vertical tectonic rates (see red and blue squares in Figure 7 a,b,c for southern and northern Italy respectively: sites that are below sea level and above 15 m are considered tectonically active or affected by subsidence because no sensible combination of ESL and GIA can explain such low / high values). However,

360 the GIA signal is significant and definitely non-negligible in the tectonically stable areas (green
361 squares).
362
363 The ocean-loading term is an important contributor to the background GIA in the Mediterranean
364 Sea. The central Mediterranean areas are affected by uplift during the MIS 6 glacial maximum in
365 response to water removal. The melt-water redistribution that follows the melting of MIS 6 ice
366 sheets causes subsidence in the bulk of the basin and results in a monotonous RSL rise during the
367 MIS 5e (Figure 6e,f). An opposite trend affects the marginal areas to the West (Morocco and
368 southern Spain; see sites no.1,2 and 4 of Figure 1, 6), where subsidence occurs during the MIS 6
369 glacial period and uplift during the MIS 5e. The latter is known as continental levering and
370 describes the upward tilt of the continental margin in response to the ocean-load-induced
371 subsidence of the center of the basin (Clark and Lingle, 1979; Stocchi and Spada, 2007). This
372 process is particularly strong at sites no. 1, 2 and 4 (Figure 6a), which are pushed upwards in
373 response to the water-load-induced central subsidence of the Mediterranean Sea and the Atlantic
374 Ocean.
375 Overall, the ocean loading-term alone results in a uniform RSL response within the Mediterranean
376 basin. The RSL variability, in fact, is mostly reduced because of the lack of the collapsing forebulge
377 around Fennoscandia. The latter is induced by the Fennoscandian ice-loading term and is
378 characterized by a strong latitudinal dependence. The crustal deformations that accompany the
379 collapse of the forebulge, in fact, decrease from north to south across the Mediterranean.
380
381 The inclusion of the ice-loading contribution from the distant ice sheets (North America, Greenland
382 and Antarctica) already results in significantly different RSL curves and in higher maximum RSL
383 elevations (see Figure 6). The predicted RSL curves at sites no.10 and 11 (Figure 6g, h) reveal an
384 interesting feedback from the ice-loading term. The latter, in fact, results in an early highstand (127
385 ka) that is then followed by RSL drop (compared dashed and solid curves of Figure 6g,h). The
386 reason for this is found in the subsidence of peripheral uplifted forebulges that surrounded the
387 formerly glaciated areas (North America, Greenland and Antarctica) at the MIS 6. As a result, water

388 moves from the far-field areas (such as eastern Mediterranean) towards the forebulge regions in
389 order to conserve the ocean mass. This process is known as ocean syphoning (Mitrovica and Milne,
390 2002) and usually adds to the continental levering. Stocchi and Spada (2007) have shown that this
391 RSL pattern can be found in the Mediterranean during the late Holocene.
392
393 The ocean- and ice-loading terms are characterized by different areal extent and interact with
394 different vertical portions of the mantle. Accordingly, the vertical gradient of viscosity is an
395 important parameter in modulating the GIA signal (Stocchi and Spada, 2007, 2009).
396 Mantle viscosity profiles with higher viscosity contrast tend to delocalize the GIA effects. This is
397 because deformation mainly happens in the upper mantle and so flow deformation – tend to stretch
398 out laterally rather then with depth. So, for the full background GIA, this results in s southwards
399 shift of the collapsing forebulge, which now interferes with the RSL changes in the Mediterranean.
400 As a result, the maximum RSL elevation occurs later and is higher in the center of the basin (sites
401 no. 7, 8).
402
403 By comparing the predicted RSL in the Mediterranean Sea with the values expected in the Gulf of
404 Biscay and in the Black Sea we can appreciate the contribution of the ice-loading term to the
405 regional RSL variability (Figure 7). By 122 ka the Gulf of Biscay and the Black Sea are
406 characterized by a sea level that is still 2-3 m below the eustatic (7.0 m). This delay is related to the
407 slow subsidence of the peripheral forebulge that uplifted around the Fennoscandia ice sheet during
408 the MIS 6. The subsidence is characterized by a clear N-S trend.
409
410 The data-models comparison shows that the differences between observations and predictions
411 generally decrease when a two-step melting chronology for AIS and GrIS (scenario 2-4) is
412 assumed and the observations divided into two age groups (before and after 122 ka). This implies
413 that the observations do not correspond to the maximum eustatic elevation, do not necessarily
414 record the local maximum RSL elevation, and that the latter does not occur at the same time
415 everywhere in the Mediterranean.

Our results are in line with those obtained by other studies that highlighted the importance of including GIA when calculating tectonics or subsidence from MIS 5e shorelines (Creveling et al., 2015; Simms et al., 2016). We remark that the GIA models we used in this study account for a limited (albeit representative of commonly used solutions) number of mantle viscosities (see Austermann et al., 2017) and a single representation of MIS 6 ice sheet configuration. The latter, if varied, may lead to significant departures in RSL predictions (Sivan et al., 2016; Dendy et al., 2017; Rohling et al., 2017). This result becomes even more interesting when the tectonic rates are extrapolated linearly through time (Figure 11). Although this should be considered as a theoretical exercise, as tectonics are never linear through time, it shows that calculating long-term (e.g. Pliocene) or recent (e.g. Holocene) tectonic stability on the basis of the MIS 5e RSL indicators can only give very general indications and must be used accordingly.

5. Conclusions

1. The observed range of MIS 5e RSL highstand from 11 tectonically stable sites in the Mediterranean is comprised between 2 and 10 m above present msl. The observed hoghstands are not necessarily coeval. Evidences of two MIS 5e RSL stands are found in Mallorca, northern Tyrrhenian coast of Italy, southeastern Sardinia and Tunisia.

2. The GIA-induced RSL changes across the Mediterranean are characterized by a significant regional variability throughout the MIS 5e. The Earth is in isostatic imbalance and a generalized RSL highstand above present sea level is predicted. The maximum highstand elevation of 2-2.5 m, which is locally predicted according to the background GIA only, is comparable to the hypothesized eustatic contribution from the GrIS as well as to the lower limit of the observations.

3. According to GIA, the MIS 5e RSL highstand occurs at different times as a function of the geographical location in the Mediterranean.

3. To precisely quantify the GrIS and AIS retreat during MIS 5e on the basis on RSL data, requires that the maximum extent, thickness and retreat of the MIS 6 ice sheets, and in particular of Fennoscandia, are constrained.

4. A two-step melting chronology where the GrIS and AIS retreat is out of phase is capable of reconciling predictions and observations provided that the GIA processes are included.

5. Neglecting the uncertainties that are related to RSL indicators and GIA may lead to over- or underestimations of local crustal motions even at sites that are considered tectonically stable. As a consequence, we suggest that caution should be exercised when extrapolating long-term tectonic rates from MIS 5e shorelines.

Acknowledgments

AR and TL's research is financially supported by: The Institutional Strategy of the University of Bremen, funded by the German Excellence Initiative [ABPZuK-03/2014]; The ZMT, the Leibniz Centre for Tropical Marine Research. The authors acknowledge USSP Urbino Summer School in Paleoclimatology (Urbino, Italy), MEDFLOOD - Modeling Paleo Processes (INQUA CMP projects 1203P and 1603P), PALSEA (PAGES/INQUA working group) and PAIS 2017 (Trieste, Italy), for the useful discussions. We are grateful to F. Antonioli, L. Carobene, M. Firpo, J.J. Fornós, E. Galili, L. Gomez-Pujol, P.J. Hearty and D. Sivan for field visits, useful discussions and insights on some of the sites mentioned in this text.

References

Angelier, J., J. P. Cadet, G. Delibrias, J. Fourniguet, M. Gigout, M. Guillemin, M. T. Hogrel, C. Lalou, and G. Pierre, 1976, Les déformations du Quaternaire marin, indicateurs néotectoniques. Quelques exemples méditerranéens: Revue de Géographie Physique et de Géologie Dynamique, v. XVIII, p. 427-448.

Antonioli, F, Dai Pra, G, Hearty, P. J., 1988. I sedimenti quaternari nella fascia costiera della Piana di Fondi (Lazio meridionale). Bollettino Societa Geologica Italiana 107, 491–501.

Antonioli, F., Ferranti, L., 1992. Geomorfologia costiera e subacquea e considerazioni paleoclimatiche sul settore compreso tra S. Maria Navarrese e Punta Goloritzé (Golfo di Orosei, Sardegna). G. di Geol. 54, 66–89.

Antonioli, F., D'Orefice, M., Ducci, S., Firmati, M., Foresi, L.M., Graciotti, R., Pantaloni, M., Perazzi, P., Principe, C., 2011. Palaeogeographic reconstruction of northern Tyrrhenian coast using archaeological and geomorphological markers at Pianosa island (Italy). Quat. Int. 232, 31–44.

Antonioli, F., Lo Presti, V., Rovere, A., Ferranti, L., Anzidei, M., Furlani, S., Mastronuzzi, G., Orru, P.E., Scicchitano, G., Sannino, G., Spampinato, C.R., Pagliarulo, R., Deiana, G., de Sabata, E., Sansò, P., Vacchi, M., Vecchio, A., 2015. Tidal notches in Mediterranean Sea: a comprehensive analysis. Quat. Sci. Rev. 119, 66–84. doi:10.1016/j.quascirev.2015.03.016

Antonioli, F., Anzidei, M., Amorosi, A., Lo Presti, V., Mastronuzzi, G., Deiana, G., De Falco, G., Fontana, A., Fontolan, G., Lisco, S., Marsico, A., Moretti, M., Orrù, P.E., Sannino, G.M., Serpelloni, E., Vecchio, A., 2017. Sea-level rise and potential drowning of the Italian coastal plains: Flooding risk scenarios for 2100. Quat. Sci. Rev. 158, 29–43. doi:10.1016/j.quascirev.2016.12.021

Anzidei, M., Lambeck, K., Antonioli, F., Furlani, S., Mastronuzzi, G., Serpelloni, E., Vannucci, G., 2014. Coastal structure, sea-level changes and vertical motion of the land in the Mediterranean. Geol. Soc. London, Spec. Publ. doi:10.1144/SP388.20

Austermann, J., Mitrovica, J.X., Huybers, P., Rovere, A., 2017. Detection of a dynamic topography signal in last interglacial sea level records. Sci. Adv. 3, e1700457.

Bardají, T., Goy, J.L., Zazo, C., Hillaire-Marcel, C., Dabrio, C.J., Cabero, A., Ghaleb, B., Silva, P.G., Lario, J., 2009. Sea level and climate changes during OIS 5e in the Western Mediterranean. Geomorphology 104, 22–37.

Benjamin, J., Rovere, A., Fontana, A., Furlani, S., Vacchi, M., Inglis, R.H.H., Galili, E., Antonioli, F., Sivan, D., Miko, S., Mourtzas, N., Felja, I., Meredith-Williams, M., Goodman-Tchernov, B., Kolaiti, E., Anzidei, M., Gehrels, R., 2017. Late Quaternary sea-level changes and early human societies in the central and eastern Mediterranean Basin: An interdisciplinary review. Quat. Int. 449, 29–57. doi:10.1016/j.quaint.2017.06.025

Carobene, L., 2015. Marine Notches and Sea-Cave Bioerosional Grooves in Microtidal Areas : Examples from the Tyrrhenian and Ligurian Coasts — Italy. J. Coast. Res. 31, 536 – 556. doi:10.2112/JCOASTRES-D-14-00068.1

Clark, J.A., Lingle, C.S., 1979. Predicted relative sea-level changes (18 000 years BP to present) caused by late-glacial retreat of Antarctic ice sheet. Quaternary Research, 11, 279-298.

Creveling, J.R., Mitrovica, J.X., Hay, C.C., Austermann, J., Kopp, R.E., 2015. Revisiting tectonic corrections applied to Pleistocene sea-level highstands. Quat. Sci. Rev. 111, 72–80. doi:10.1016/j.quascirev.2015.01.003

De Boer, B., Stocchi, P., Van De Wal, R., others, 2014. A fully coupled 3-D ice-sheet-sea-level model: algorithm and applications. Geosci. Model Dev. 7, 2141–2156.

Deconto, R.M., Pollard, D., 2016. Contribution of Antarctica to past and future sea-level rise. Nature 531, 591–597. doi:10.1038/nature17145

Dendy, S., Austermann, J., Creveling, J.R., Mitrovica, J.X., 2017. Sensitivity of Last Interglacial sea-level high stands to ice sheet configuration during Marine Isotope Stage 6. Quat. Sci. Rev. 171, 234–244. doi:10.1016/j.quascirev.2017.06.013

Düsterhus, A., Rovere, A., Carlson, A.E., Horton, B.P., Klemann, V., Tarasov, L., Barlow, N.L.M., Bradwell, T., Clark, J., Dutton, A., Gehrels, W.R., Hibbert, F.D., Hijma, M.P., Khan, N., Kopp, R.E., Sivan, D., Törnqvist, T.E., 2016. Palaeo-sea-level and palaeo-ice-sheet databases: problems, strategies, and perspectives. Clim. Past 12, 911–921. doi:10.5194/cp-12-911-2016

Dutton, A., Lambeck, K., 2012. Ice Volume and Sea Level During the Last Interglacial. Science 337, 216–219. doi:10.1126/science.1205749

Dutton, A., Carlson, A.E.E., Long, A.J.J., Milne, G.A.A., Clark, P.U.U., DeConto, R., Horton, B.P., Rahmstorf, S., Raymo, M.E., 2015. Sea-level rise due to polar ice-sheet mass loss during past warm periods. Science 349, aaa4019-aaa4019. doi:10.1126/science.aaa4019

Faccenna, C., Becker, T.W., Auer, L., Billi, A., Boschi, L., Brun, J.P., Capitanio, A.A., Funicello, F., Horvàt, F., Jolivet, L., Piromallo, C., Royden, L., Rossetti, F., and Serpelloni, E., 2014.

525 Mantle dynamics in the Mediterranean. Reviews of Geophysics,
526 doi:10.1002/2013RG000444
527 Farrell, W.E., Clark, J.A., 1976. On postglacial sea level. Geophys. J. Int. 46, 647–667.
528 doi:10.1111/j.1365-246X.1976.tb01252.x
529 Federici, P.R., Pappalardo, M., 2006. Evidence of Marine Isotope Stage 5.5 highstand in Liguria
530 (Italy) and its tectonic significance. Quat. Int. 145–146, 68–77.
531 Ferranti, L., Antonioli, F., Mauz, B., Amorosi, A., Dai Pra, G., Mastronuzzi, G., Monaco, C., Orrù,
532 P., Pappalardo, M., Radtke, U., Renda, P., Romano, P., Sansò, P., Verrubbi, V., 2006.
533 Markers of the last interglacial sea-level high stand along the coast of Italy: Tectonic
534 implications. Quat. Int. 145–146, 30–54.
535 Galili, E., Zviely, D., Ronen, A., Mienis, H.K., 2007. Beach deposits of MIS 5e high sea stand as
536 indicators for tectonic stability of the Carmel coastal plain, Israel. Quat. Sci. Rev. 26, 2544–
537 2557. doi:10.1016/j.quascirev.2007.06.027|ISSN 0277-3791
538 Goy, J. L., C. Zazo, T. Bardaji, L. Somoza, C. Causse, and C. Hillaire Marcel, 1993, Eléments
539 d'une chronostratigraphie du Tyrrhénien des régions d'Alicante-Murcie, Sud-Est de
540 l'Espagne: Geodinamica Acta, v. 6, p. 103-119.
541 Graciotti, R., Foresi, L.M., Pantaloni, M., 2002. Caratteristiche geomorfologiche dell'Isola di
542 Pianosa (Arcipelago toscano). Atti Soc. toscana di Sci. Nat. Mem., Ser. A 108, 95–111.
543 Hearty, P.J., 1986. An inventory of last interglacial (s.l.) age deposits from the Mediterranean basin:
544 a study in isoleucine epimerization and U-series dating. Zeitschrift fur Geomorphol.
545 Supplement, 62, 51–69.
546 Hearty, P.J., Hollin, J.T., Neumann, a. C., O'leary, M.J., McCulloch, M., O'Leary, M.J., 2007.
547 Global sea-level fluctuations during the Last Interglaciation (MIS 5e). Quat. Sci. Rev. 26,
548 2090–2112. doi:10.1016/j.quascirev.2007.06.019
549 Hibbert, F.D., Rohling, E.J., Dutton, A., Williams, F.H., Chutcharavan, P.M., Zhao, C., Tamisiea,
550 M.E., 2016. Coral indicators of past sea-level change: A global repository of U-series dated
551 benchmarks. Quat. Sci. Rev. 145, 1–56. doi:10.1016/j.quascirev.2016.04.019

552 Hijma, M.P., Engelhart, S.E., Törnqvist, T.E., Horton, B.P., Hu, P., Hill, D.F., 2015. A protocol for
553 a geological sea-level database, in: Shennan, I., Long, A.J., Horton, B.P. (Eds.), Handbook
554 of Sea-Level Research. Wiley Online Library, pp. 536–553.
555 doi:10.1002/9781118452547.ch34
556 Lambeck, K., Purcell, A., 2005. Sea-level change in the Mediterranean Sea since the LGM: model
557 predictions for tectonically stable areas. Quaternary Science Reviews, 24, 1969-1988.
558 Lorscheid, T., Stocchi, P., Casella, E., Gómez-Pujol, L., Vacchi, M., Mann, T., Rovere, A., 2017.
559 Paleo sea-level changes and relative sea-level indicators: Precise measurements, indicative
560 meaning and glacial isostatic adjustment perspectives from Mallorca (Western
561 Mediterranean). Palaeogeogr. Palaeoclimatol. Palaeoecol. 473, 94–107.
562 doi:10.1016/j.palaeo.2017.02.028
563 Mauz, B., Antonioli, F., 2009. Comment on "Sea level and climate changes during OIS 5e in the
564 Western Mediterranean" by T. Bardají, J.L. Goy, J.L., C. Zazo, C. Hillaire-Marcel, C.J.
565 Dabrio, A. Cabero, B. Ghaleb, P.G. Silva, J. Lario, Geomorphology 104 (2009), 22–37.
566 Geomorphology 110, 227–230.
567 Mauz, B., Fanelli, F., Elmejdoub, N., Barbieri, R., 2012. Coastal response to climate change:
568 Mediterranean shorelines during the Last Interglacial (MIS 5). Quat. Sci. Rev. 1–10.
569 Mitrovica, J.X., Peltier, W.R., 1991. On postglacial geoid subsidence over the equatorial oceans. J.
570 Geophys. Res. Solid Earth 96, 20053–20071. doi:10.1029/91JB01284
571 Mitrovica, J.X., Milne, G.A., 2002. On the origin of late Holocene sea-level highstands within
572 equatorial ocean basins. Quat. Sci. Rev. 21, 2179–2190.
573 Muhs, D.R., Simmons, K.R., Meco, J., Porat, N., 2015. Uranium-series ages of fossil corals from
574 Mallorca, Spain: The "Neotyrrhenian" high stand of the Mediterranean Sea revisited.
575 Palaeogeogr. Palaeoclimatol. Palaeoecol. 438, 408–424. doi:10.1016/j.palaeo.2015.06.043
576 Murray-Wallace, C. V, Belperio, A.P., 1991. The last interglacial shoreline in Australia—a review.
577 Quat. Sci. Rev. 10, 441–461.

O'Leary, M.J., Hearty, P.J., Thompson, W.G., Raymo, M.E., Mitrovica, J.X., Webster, J.M., 2013. Ice sheet collapse following a prolonged period of stable sea level during the last interglacial. Nat. Geosci. 6, 796–800. doi:10.1038/ngeo1890

Paskoff, R., Sanlaville, P., 1983. Les cotes de la Tunisie: variations du niveau marin depuis le Tyrrhenien. Collect. LA MAISON L'ORIENT MÉDITERRANÉEN 14.

Pedoja, K., Husson, L., Johnson, M.E., Melnick, D., Witt, C., Pochat, S.S., Nexer, M.M., Delcaillau, B., Pinegina, T., Poprawski, Y., Authemayou, C., Elliot, M., Regard, V., Garestier, F., 2014. Coastal staircase sequences reflecting sea-level oscillations and tectonic uplift during the Quaternary and Neogene. Earth-Science Rev. 132, 13–38. doi:10.1016/j.earscirev.2014.01.007

Peltier, W.R., 2004. Global glacial isostasy and the surface of the ice-age Earth: The ICE-5G (VM2) model and GRACE. Annu. Rev. Earth Planet. Sci. 32, 111–149.

Raymo, M.E., Mitrovica, J.X., O'leary, M.J., DeConto, R.M., Hearty, P.J., 2011. Departures from eustasy in Pliocene sea-level records. Nat. Geosci. 4, 328–332.

Rohling, E.J., Hibbert, F.D., Williams, F.H., Grant, K.M., Marino, G., Foster, G.L., Hennekam, R., de Lange, G.J., Roberts, A.P., Yu, J., Webster, J.M., Yokoyama, Y., 2017. Differences between the last two glacial maxima and implications for ice-sheet, δ18O, and sea-level reconstructions. Quat. Sci. Rev. 176, 1–28. doi:10.1016/j.quascirev.2017.09.009

Rovere, A., Antonioli, F., Bianchi, C.N., 2015. Fixed biological indicators, in: Shennan, I., Long, A.J., Horton, B.P. (Eds.), Handbook of Sea-Level Research. Wiley Online Library, pp. 268–280.

Rovere, A., Raymo, M.E., Vacchi, M., Lorscheid, T., Stocchi, P., Gómez-Pujol, L., Harris, D.L., Casella, E., O'Leary, M.J., Hearty, P.J., 2016a. The analysis of Last Interglacial (MIS 5e) relative sea-level indicators: Reconstructing sea-level in a warmer world. Earth-Science Rev. 159, 404–427. doi:10.1016/j.earscirev.2016.06.006

Rovere, A., Stocchi, P., Vacchi, M., 2016b. Eustatic and Relative Sea Level Changes. Curr. Clim. Chang. Reports 2, 221–231. doi:10.1007/s40641-016-0045-7

605 Shennan, I., 1982. Interpretation of Flandrian sea-level data from the Fenland, England. Proc. Geol.
606 Assoc. 83, 53–63. doi:10.1016/S0016-7878(82)80032-1
607 Shennan, I., 1989. Holocene crustal movements and sea-level changes in Great Britain. J. Quat. Sci.
608 4, 77–89. doi:10.1002/jqs.3390040109
609 Shennan, I., Horton, B., 2002. Holocene land- and sea-level changes in Great Britain. J. Quat. Sci.
610 17, 511–526.
611 Shennan, I., Long, A.J., Horton, B.P., 2014. Handbook of Sea-level Research. Wiley Online
612 Library.
613 Simms, A.R., Rouby, H.H., Lambeck, K., 2016. Marine terraces and rates of vertical tectonic
614 motion: The importance of glacio-isostatic adjustment along the Pacific coast of central
615 North America. Bull. Geol. Soc. Am. 128, 81–93. doi:10.1130/B31299.1
616 Sivan, D., Sisma-Ventura, G., Greenbaum, N., Bialik, O.M., Williams, F.H., Tamisiea, M.E.,
617 Rohling, E.J., Frumkin, A., Avnaim-Katav, S., Shtienberg, G., Stein, M., 2016. Eastern
618 Mediterranean sea levels through the last interglacial from a coastal-marine sequence in
619 northern Israel. Quat. Sci. Rev. 145, 204–225. doi:10.1016/j.quascirev.2016.06.001
620 Spada, G., Stocchi, P., 2007. SELEN: A Fortran 90 program for solving the “sea-level equation.”
621 Comput. Geosci. 33, 538–562.
622 Stocchi, P., and Spada, G., 2007. Glacio and hydro-isostasy in the Mediterranean Sea: Clark's zones
623 and role of remote ice sheets. Annals of Geophysics, 50, 741-761.
624 Stocchi, P., and Spada, G., 2009. Influence of glacial isostatic adjustment upon current sea level
625 variations in the Mediterranean. Tectonophysics, 474, 56-68.
626 Stocker, T.F., Qin, D., Plattner, G.-K., Tignor, M., Allen, S.K., Boschung, J., Nauels, A., Xia, Y.,
627 Bex, V., Midgley, P.M., 2013. Climate Change 2013. The Physical Science Basis. Working
628 Group I Contribution to the Fifth Assessment Report of the Intergovernmental Panel on
629 Climate Change-Abstract for decision-makers.
630 Suess, E., 1906. The Face of the Earth, vol. 2, F. Tempsky, Vienna.
631 Ulzega, A., Hearty, P.J., 1986. Geomorphology, stratigraphy and geochronology of Late Quaternary
632 marine deposits in Sardinia. Zeitschrift für Geomorphol. Suppl. Bd., 119–129.

633 Vacchi, M., Marriner, N., Morhange, C., Spada, G., Fontana, A., Rovere, A., Marriner, N.,
634 Morhange, C., Spada, G., Fontana, A., 2016. Multiproxy assessment of Holocene relative
635 sea-level changes in the western Mediterranean: variability in the sea-level histories and
636 redefinition of the isostatic signal. Earth Sci. Rev. 155, 172–197.
637 doi:10.1016/j.earscirev.2016.02.002
638 Van de Plassche, O., 1986. Sea-level research: a manual for the collection and evaluation of data: A
639 manual for the collection and evaluation of data. Springer. doi:10.1007/978-94-009-4215-
640 8_15
641 Zazo, C., Goy, J.L., Dabrio, C.J., Bardají, T., Hillaire-Marcel, C., Ghaleb, B., González-Delgado,
642 J.-Á., Soler, V., Bardají, T., Hillaire-Marcel, C., Ghaleb, B., González-Delgado, J.-Á.,
643 Soler, V., 2003. Pleistocene raised marine terraces of the Spanish Mediterranean and
644 Atlantic coasts: records of coastal uplift, sea-level highstands and climate changes. Mar.
645 Geol. 194, 103–133.
646 Zazo, C., Goy, J.L.L., Dabrio, C.J.J., Lario, J., González-Delgado, J. a. A., Bardají, T., Hillaire-
647 Marcel, C., Cabero, a., Ghaleb, B., Borja, F., Silva, P.G.G., Roquero, E., Soler, V., 2013.
648 Retracing the Quaternary history of sea-level changes in the Spanish Mediterranean–
649 Atlantic coasts: Geomorphological and sedimentological approach. Geomorphology 196,
650 36–49. doi:10.1016/j.geomorph.2012.10.020
651

652 **Figures and Tables captions**

653 **Figure 1.** Tectonics map of the Mediterranean Sea and geographical locations of the 11 RSL sites
654 that considered in this study. Faults are modified after Faccenna et al. (2014). Site names: 1-
655 Morocco-Al Hoceima; 2- Italy-Pianosa; 3- Spain-Cala Blava; 4- Italy-Bergeggi; 5- Italy-Pianosa; 6-
656 Italy-Pisco Montano; 7- Italy-Cala Luna; 8- Italy-Cala Mosca; 9- Tunisia-Hergla-S; 10- Libia-W
657 Libia; 11- Israel-Nahal Galim.

658 **Figure 2.** Geological sketches of some of the eleven MIS 5e Mediterranean sites reviewed in this
659 study (see Figure 1 for location). a) Site 9 - MIS 5e beach deposits, Hergla South, Tunisia (redrawn
660 and adapted from Paskoff and Sanlaville, 1983); b) Site 11 - MIS 5e beach deposits, Nahal Galim,

661 Israel; c) Site 8 - MIS 5e beach deposits, Cala Mosca, Sardinia, Italy (redrawn from Hearty, 1986);
662 d) Site 6 - Tidal notch and associated deposits, Pisco Montano, Italy; e) Site 3 - MIS 5e beach
663 deposits, Cala Blava, Mallorca, Spain; f) Site 5 – Biological sea level markers and MIS 5e beach
664 deposits, Pianosa, Italy; g) Measured RSL marker (black line) vs paleo RSL elevation (blue band)
665 for all the locations shown in Figure 1 (letters indicate the outcrops described in a-f). References for
666 sites in g): **Site 1** - Angelier et al, 1976; **Site 2** - Mauz & Antonioli, 2009; Bardajii et al., 2009;
667 Zazo et al., 2003; Goy et al., 1993; **Site 3** - Zazo et al., 2003; Zazo et al., 2013; Lorscheid et al.,
668 2015; Hearty, 1986; Muhs et al., 2015; **Site 4** - Carobene et al., 2014; Ferranti et al., 2006; Federici
669 and Pappalardo, 2006; **Site 5** - Antonioli et al., 2011; Graciotti et al., 2002; **Site 6** - Antonioli et al.,
670 1998; **Site 7** - Antonioli & Ferranti, 1992; **Site 8** - Ulzega and Hearty, 1986; Hearty, 1986; **Site 9** -
671 Hearty et al., 2007; Paskoff and Sanlaville, 1983; **Site 10** - Pedoja et al., 2014; **Site 11** - Galili et al.,
672 2007; Mauz et al., 2012.
673 **Figure 3.** GrIS and AIS melting scenarios reflecting the uncertainties in MIS5e glacioeustatic
674 contributions (m ESL). See text for the description of each scenario.
675 **Figure 4.** Predicted maximum RSL elevation between 127 and 116 ka for the background GIA and
676 according to MVP1 (red), MVP2 (green) and MVP3 (blue). The predicted values are computed
677 along the transect connecting the sites shown in Figure 1 from West to East. Colored squares
678 correspond to the 11 investigated sites mapped in Figure 1.
679 **Figure 5.** Predicted RSL curves at each of the 11 sites of Figure 1 according to the background
680 GIA. Red, green and blue colors stem for, respectively, MVP1, 2 and 3 (a-c). Thick solid curve
681 represents site no. 1 (Al Hoceima, Morocco); thick dotted curve represents site no.4 (Bergeggi,
682 Italy); Cala Mosca (Italy); thick dashed curve represents site no.8 (Cala Mosca, Sardinia, Italy). The
683 black thin solid curves represent the remaining 8 sites for the three MVPs and show the spatio-
684 temporal variability of GIA in the area.
685 **Figure 6.** The role of ocean- and ice-loading terms. a) predicted maximum RSL elevation according
686 to background GIA and considering the ocean-loading term only (i.e. the ice-loading term is
687 neglected); b) predicted maximum RSL elevation according to background GIA and neglecting the

ice-loading term for the Eurasian ice-sheets aggregate only; c-h) RSL curves at 6 sites according to a (solid curves) and b (dashed curves). See text for explanations.

Figure 7. Predicted RSL elevation at 122 ka according to glacioeustatic scenario 1 and MVP1-3 (a-c). The colored squared indicate the elevation of MIS5e markers (Pedoja et al., 2014). According to the eustatic approximation, scenario 1 would result in a 7.0 m highstand. However, background GIA combined with the GIA that accompanies and follows the melting of GrIS and AIS (scenario 1) results in a regionally varying RSL at 122 ka. According to MVP1, the predicted RSL exceeds the eustatic value along the northern coasts on the Mediterranean basin (a). Moving toward larger viscosity gradients between upper mantle and lower mantle (b-c) results in lower RSL elevation at 122 ka.

Figure 8. Predicted RSL curves at sites no.1, 4, 5, 7 and 10 according to scenario 1 (blue curve), scenario 2 (pink curve), scenario 3 (black curve), scenario 4 (green curve), background GIA (dotted black curve) and for MVP2.

Figure 9. Predictions vs observations: chi-square estimator. a) chi-square as function of mantle viscosity profile and glacioeustatic scenarios (1-3) and using the highest observed sea level (if there is more than one as in sites no.3, 5, 8 and 9) at each RSL site (see Figure 1, 2) and comparing it to the highest predicted RSL; b) same as (a) but assuming that, where there is one observed sea level only, if it is above or below 5.0 m it is the maximum attained sea level after or before 122 ka respectively. Where two sea levels are observed (sites no.3, 5, 8 and 9), the lower one represents the maximum sea level before 122 ka while the higher one represents the maximum sea level after 122 ka. For scenario 4 the order is inverted in order to be consistent with the ice-sheets chronology (higher peak first, then followed by lower peak).

Figure 10. Histograms showing the relative frequency of the post-depositional rates (PDr) calculated for the 11 Mediterranean sites addressed in this study. Blue histograms show the PDr calculated using the GIA+ESL correction presented in this paper. Gray histograms show the PDr calculated using ESL=6m. The last panel on the lower right shows the cumulative relative frequency for all sites. At sites 3,5,8,9 the histograms represent the results of the calculation of PDr using two RSL indicators.

716 **Figure 11.** Example of extrapolation of the PDr shown in Figure 10 for two Mediterranean sites:
717 Pianosa (5) and Cala Luna (7). The lower panels represent details of the upper ones. MPWP = Mid
718 Pliocene Warm Period (Raymo et al., 2011). The blue bands represent the maximum-minimum
719 uplift/subsidence calculated using the GIA+ESL predictions, while the dashed bands represent the
720 uplift/subsidence calculated using ESL=6m in Eq. (2).
721 **Table 1.** Mantle viscosity profiles (MVP1-3) characterized by different UM, TZ and LM viscosity
722 values. The depth of UM/TZ boundary is 400 km; The depth of TZ/LM boundary is 670 km. The
723 depth of LM/outer core boundary is 3480 km. MVP1 is a simplification of the original VM1
724 (Peltier, 1996). MVP2 is a simplification of the VM2 profile that is usually employed with the ICE-
725 5G ice-sheet model (Peltier, 2004); MVP3 follows the mantle viscosity profile used by Lambeck et
726 al. (2004).

Figure 1

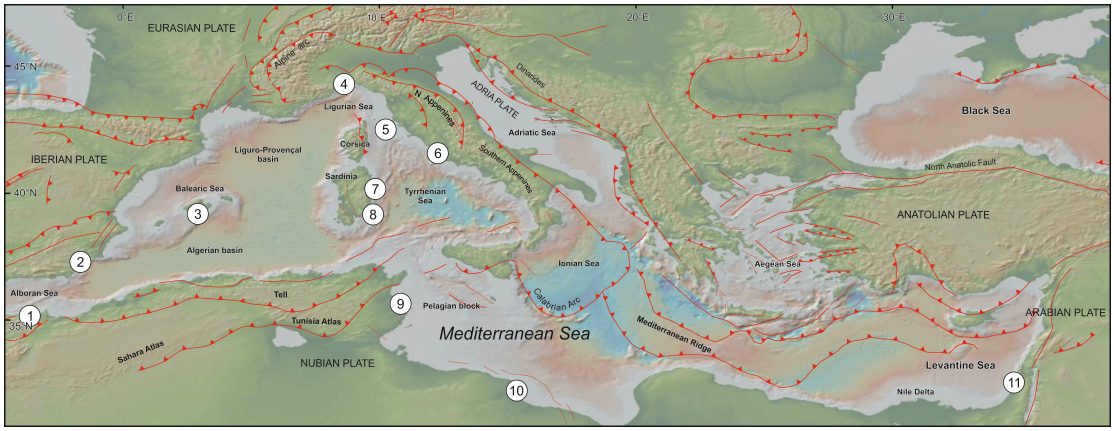
0°E
10°E
20°E
30°E
45°N
40°N
35°N
EURASIAN PLATE
Alpine arc
Dinarides
ADRIA PLATE
N. Apennines
Ligurian Sea
Adriatic Sea
Corsica
Liguro-Provençal basin
Southern Apennines
IBERIAN PLATE
Sardinia
Balearic Sea
Tyrrhenian Sea
Black Sea
North Anatolic Fault
ANATOLIAN PLATE
Algerian basin
Ionian Sea
Aegean Sea
Alboran Sea
Tell
Pelagian block
Calabrian Arc
Tunisia Atlas
Mediterranean Sea
Mediterranean Ridge
ARABIAN PLATE
Sahara Atlas
NUBIAN PLATE
Levantine Sea
Nile Delta
1
2
3
4
5
6
7
8
9
10
11

Figure 2

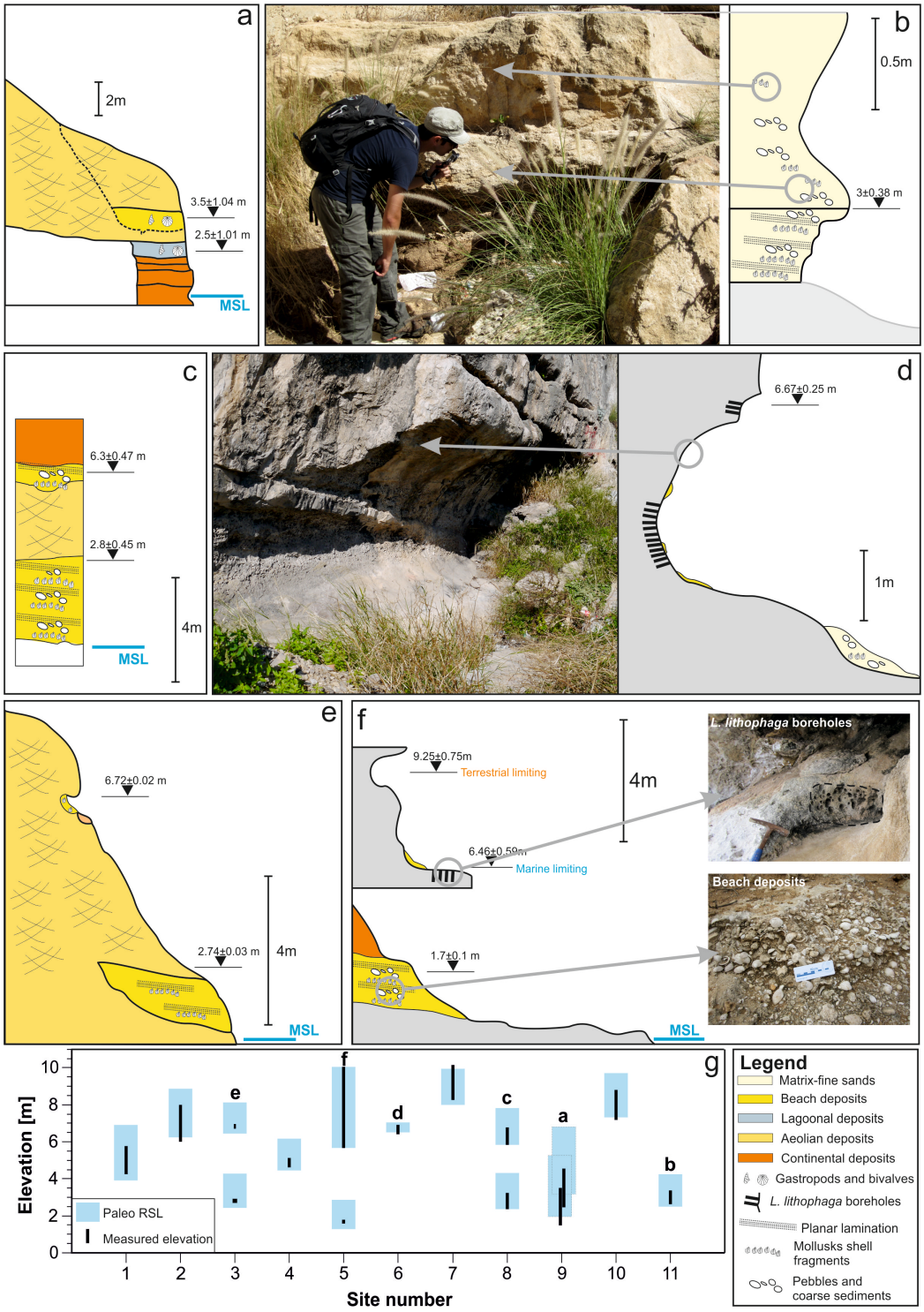
a
2m
3.5±1.04 m
2.5±1.01 m
MSL
b
0.5m
3±0.38 m
c
6.3±0.47 m
2.8±0.45 m
4m
MSL
d
6.67±0.25 m
1m
e
6.72±0.02 m
2.74±0.03 m
4m
MSL
f
9.25±0.75m
Terrestrial limiting
4m
6.46±0.59m
Marine limiting
1.7±0.1 m
MSL
L. lithophaga boreholes
Beach deposits
g
Elevation [m]
Site number
Paleo RSL
Measured elevation
Legend
Matrix-fine sands
Beach deposits
Lagoonal deposits
Aeolian deposits
Continental deposits
Gastropods and bivalves
L. lithophaga boreholes
Planar lamination
Mollusks shell fragments
Pebbles and coarse sediments

Figure 3

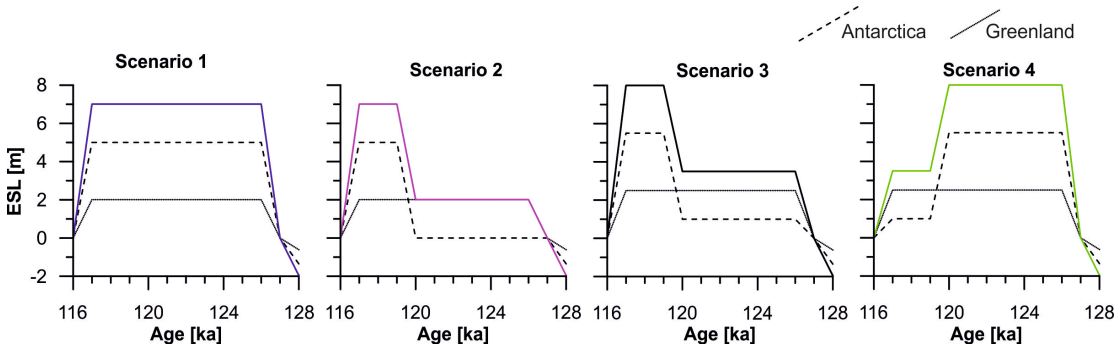
Antarctica
Greenland
Scenario 1
Scenario 2
Scenario 3
Scenario 4
ESL [m]
8
6
4
2
0
-2
116
120
124
128
Age [ka]

Figure 4

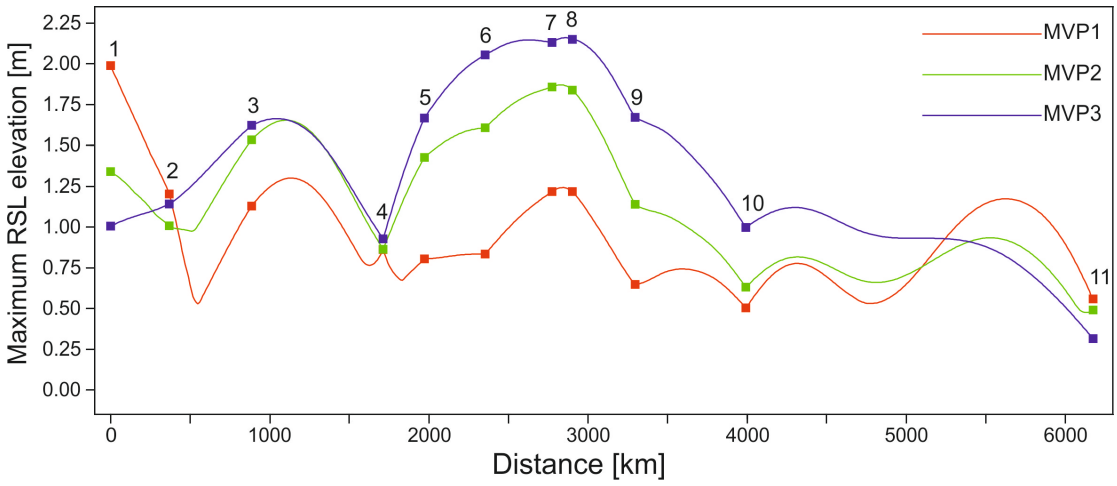
Maximum RSL elevation [m]
2.25
2.00
1.75
1.50
1.25
1.00
0.75
0.50
0.25
0.00
0
1000
2000
3000
4000
5000
6000
Distance [km]
MVP1
MVP2
MVP3
1
2
3
4
5
6
7
8
9
10
11

Figure 5

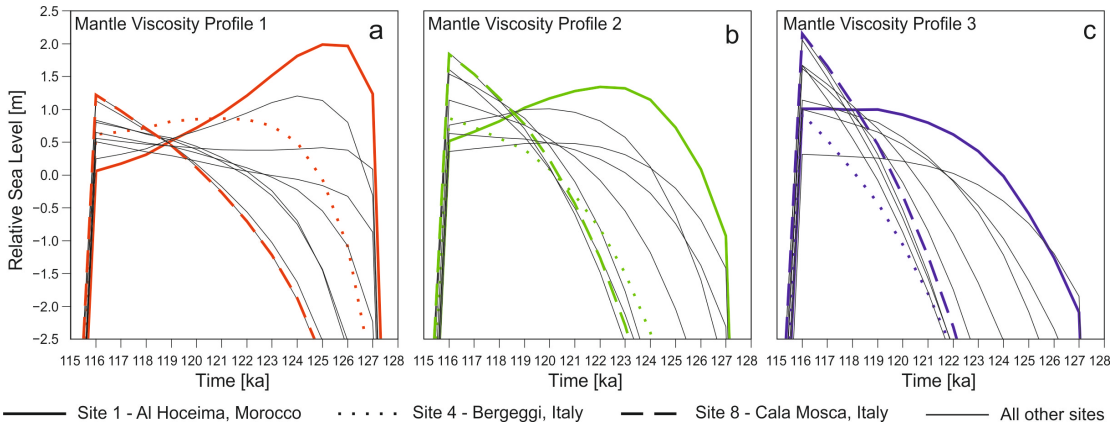
Mantle Viscosity Profile 1
a
Mantle Viscosity Profile 2
b
Mantle Viscosity Profile 3
c
Relative Sea Level [m]
2.5
2.0
1.5
1.0
0.5
0.0
−0.5
−1.0
−1.5
−2.0
−2.5
115 116 117 118 119 120 121 122 123 124 125 126 127 128
Time [ka]
Site 1 - Al Hoceima, Morocco
Site 4 - Bergeggi, Italy
Site 8 - Cala Mosca, Italy
All other sites

Figure 6

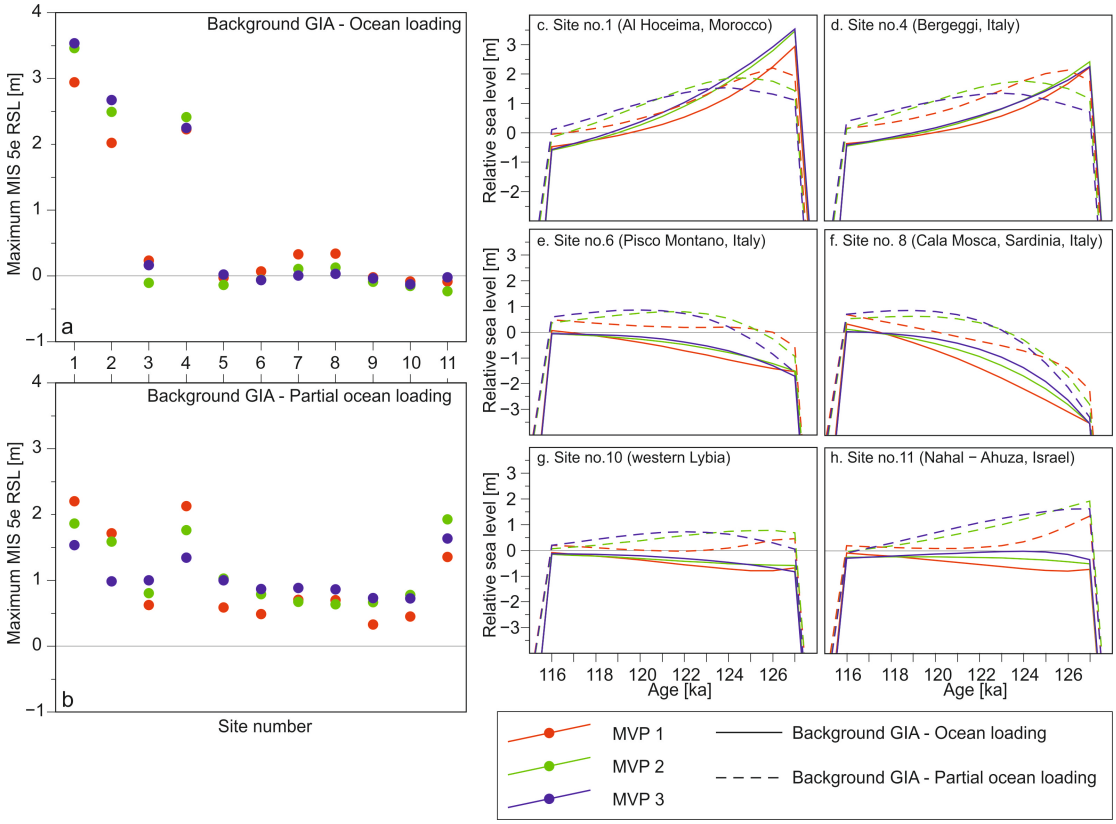
Background GIA - Ocean loading
Maximum MIS 5e RSL [m]
a
Background GIA - Partial ocean loading
Maximum MIS 5e RSL [m]
b
Site number
c. Site no.1 (Al Hoceima, Morocco)
d. Site no.4 (Bergeggi, Italy)
e. Site no.6 (Pisco Montano, Italy)
f. Site no. 8 (Cala Mosca, Sardinia, Italy)
g. Site no.10 (western Lybia)
h. Site no.11 (Nahal − Ahuza, Israel)
Relative sea level [m]
Age [ka]
MVP 1
MVP 2
MVP 3
Background GIA - Ocean loading
Background GIA - Partial ocean loading

Figure 7

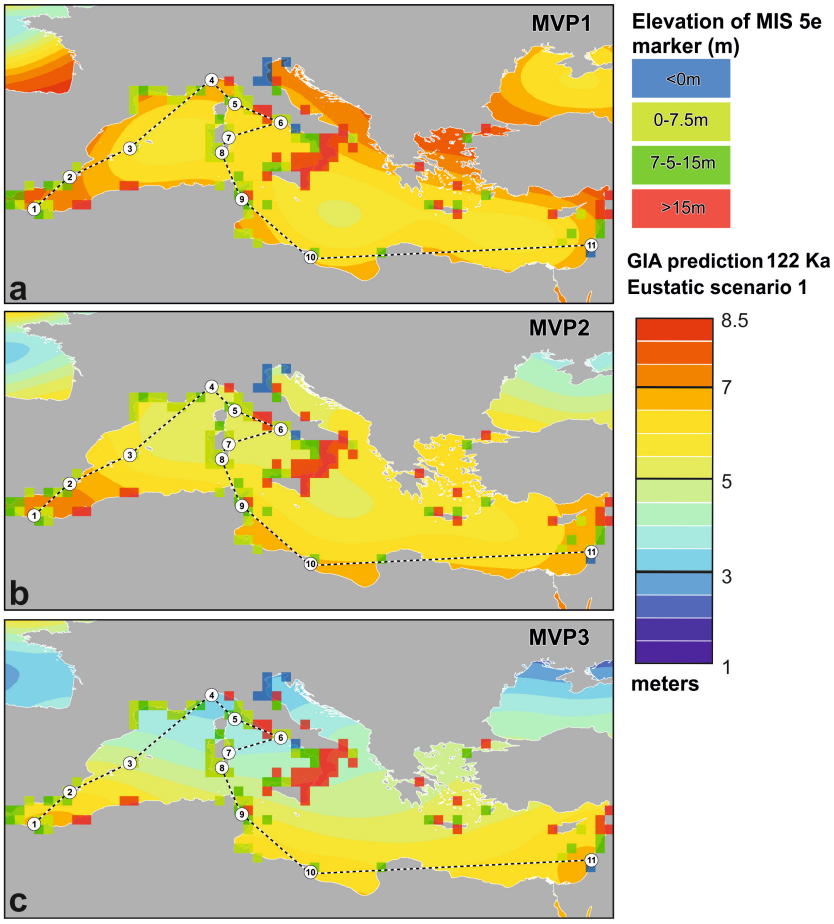
MVP1
a
MVP2
b
MVP3
c
Elevation of MIS 5e marker (m)
<0m
0-7.5m
7-5-15m
>15m
GIA prediction 122 Ka
Eustatic scenario 1
8.5
7
5
3
1
meters

Figure 8

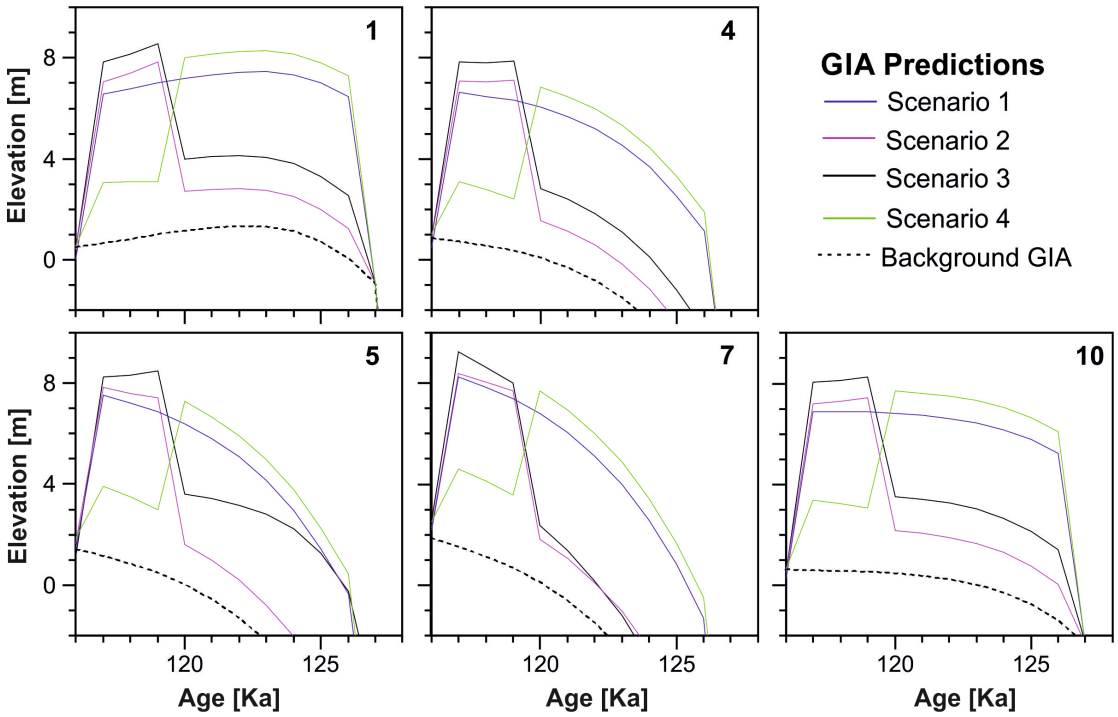
1
4
5
7
10
Elevation [m]
0
4
8
120
125
Age [Ka]
GIA Predictions
Scenario 1
Scenario 2
Scenario 3
Scenario 4
Background GIA

Figure 9

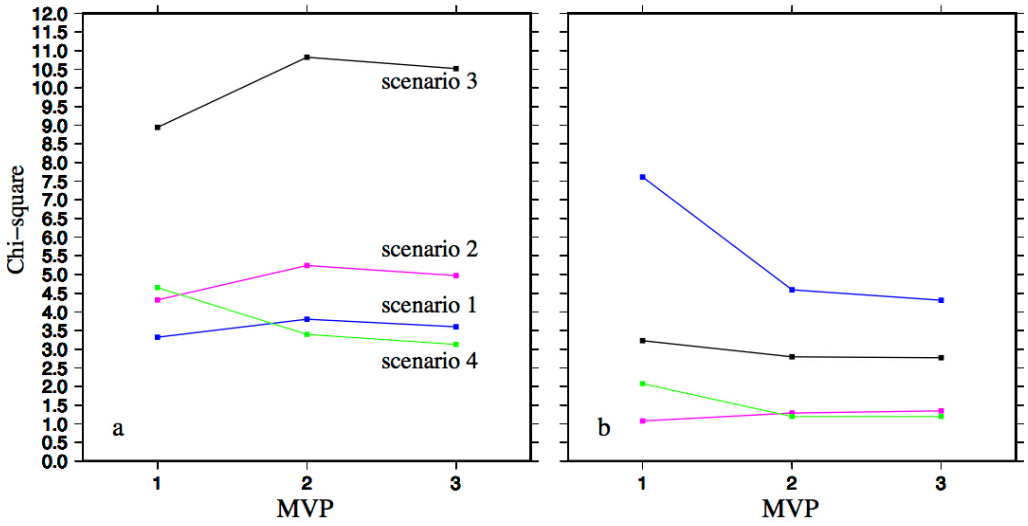
Chi−square
12.0
11.5
11.0
10.5
10.0
9.5
9.0
8.5
8.0
7.5
7.0
6.5
6.0
5.5
5.0
4.5
4.0
3.5
3.0
2.5
2.0
1.5
1.0
0.5
0.0
scenario 3
scenario 2
scenario 1
scenario 4
a
b
1
2
3
MVP
1
2
3
MVP

Figure 10

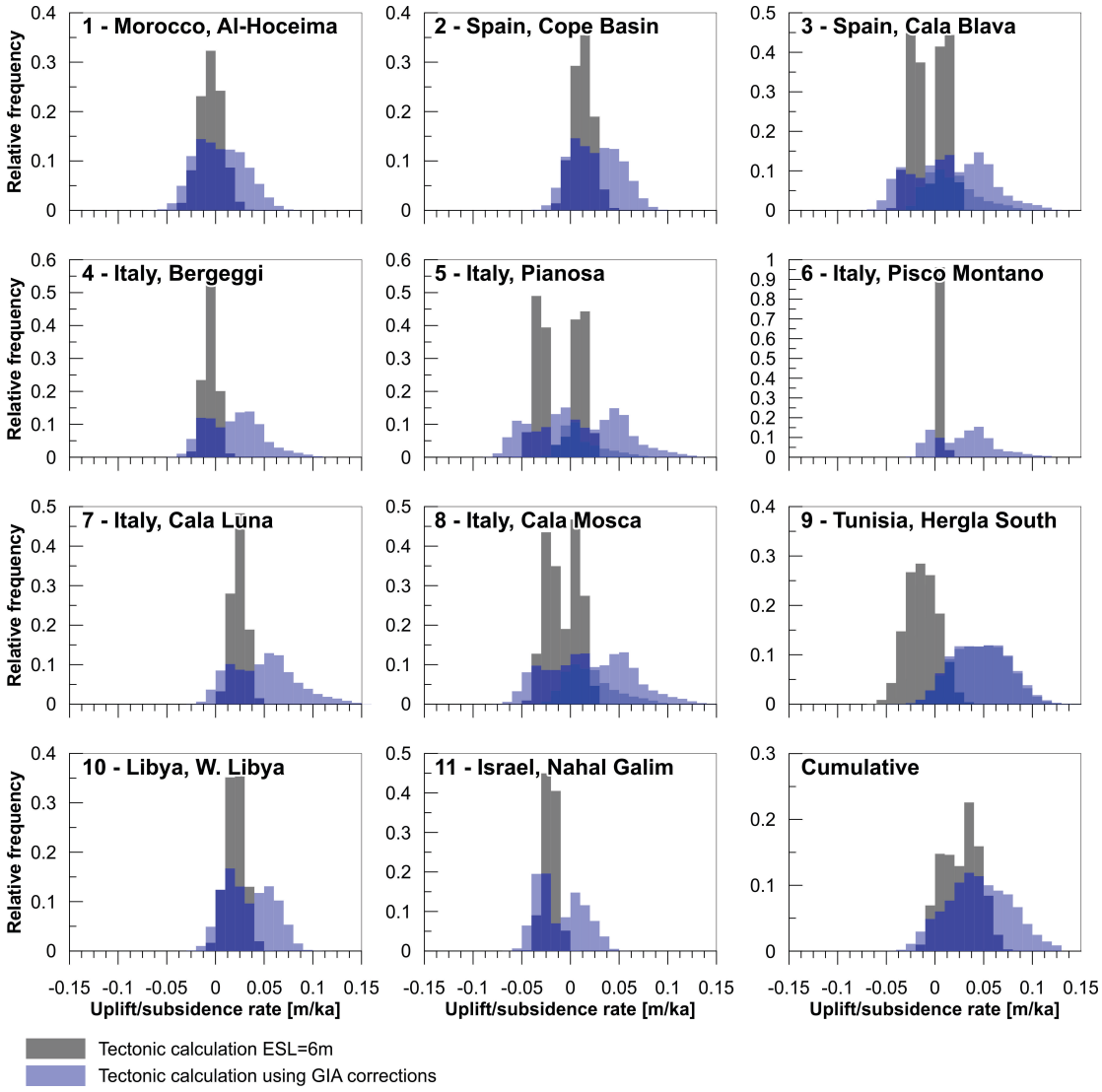
1 - Morocco, Al-Hoceima
2 - Spain, Cope Basin
3 - Spain, Cala Blava
4 - Italy, Bergeggi
5 - Italy, Pianosa
6 - Italy, Pisco Montano
7 - Italy, Cala Luna
8 - Italy, Cala Mosca
9 - Tunisia, Hergla South
10 - Libya, W. Libya
11 - Israel, Nahal Galim
Cumulative
Relative frequency
Uplift/subsidence rate [m/ka]
Tectonic calculation ESL=6m
Tectonic calculation using GIA corrections

Figure 11

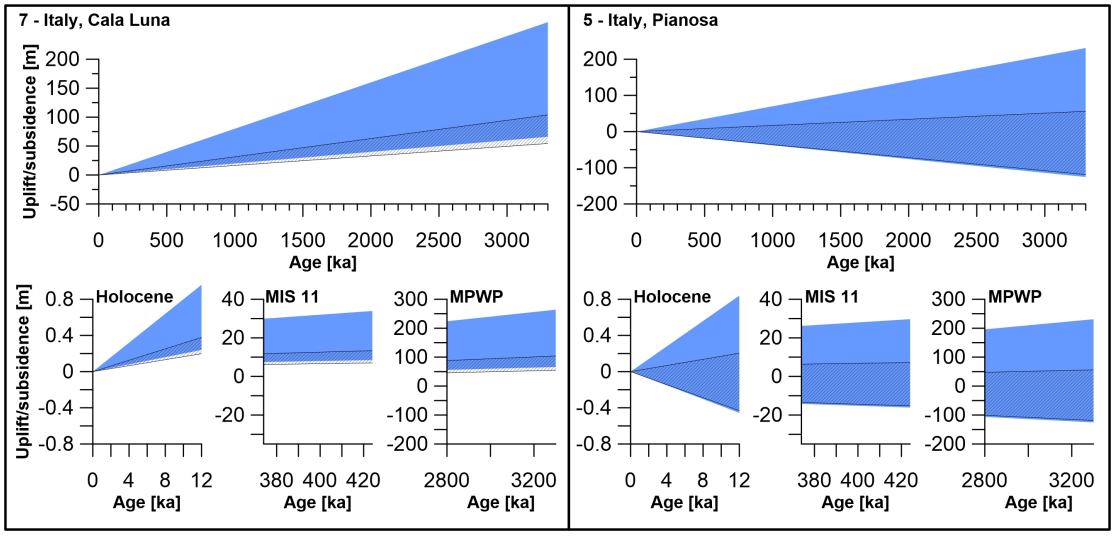
7 - Italy, Cala Luna
Uplift/subsidence [m]
200
150
100
50
0
-50
0
500
1000
1500
2000
2500
3000
Age [ka]
Uplift/subsidence [m]
Holocene
0.8
0.4
0
-0.4
-0.8
0
4
8
12
Age [ka]
MIS 11
40
20
0
-20
380
400
420
Age [ka]
MPWP
300
200
100
0
-100
-200
2800
3200
Age [ka]
5 - Italy, Pianosa
200
100
0
-100
-200
0
500
1000
1500
2000
2500
3000
Age [ka]
Holocene
0.8
0.4
0
-0.4
-0.8
0
4
8
12
Age [ka]
MIS 11
40
20
0
-20
380
400
420
Age [ka]
MPWP
300
200
100
0
-100
-200
2800
3200
Age [ka]

Table 1

	UM $x10^{21}$ Pa•s	TZ $x10^{21}$ Pa•s	LM $x10^{21}$ Pa•s
MVP1	1.0	1.0	2.0
MVP2	0.5	0.5	5.0
MVP3	0.25	0.5	10.0